LLNL-JRNL-676588

An Ensemble Constrained Variational Analysis of Atmospheric Forcing Data and Its Application to Evaluate Clouds in CAM5

S. Tang, M. Zhang, S. Xie

August 26, 2015

Journal of Geophysical Research: Atmosphere

Disclaimer

An Ensemble Constrained Variational Analysis of Atmospheric Forcing Data and Its Application to Evaluate Clouds in CAM5

Shuaiqi Tang[1,2], Minghua Zhang[1] and Shaocheng Xie[2]

1. School of Marine and Atmospheric Sciences

Stony Brook University, Stony Brook, New York, USA.

2. Lawrence Livermore National Laboratory, Livermore, California, USA

To be submitted to the *Journal of Geophysical Research*

September 2015

Corresponding Author: Shuaiqi Tang, Atmospheric, Earth, and Energy Division (L-103), Lawrence Livermore National Laboratory, Livermore, CA 94550.
E-mail: tang32@llnl.gov

Abstract

Large-scale atmospheric forcing data can greatly impact the simulations of atmospheric process models including Large Eddy Simulations (LES), Cloud Resolving Models (CRMs) and Single-Column Models (SCMs), and impact the development of physical parameterizations in global climate models. This study describes the development of an ensemble variationally constrained objective analysis of atmospheric large-scale forcing data and its application to evaluate the cloud biases in the Community Atmospheric Model (CAM5). Sensitivities of the variational objective analysis to background data, error covariance matrix and constraint variables are described and used to quantify the uncertainties in the large-scale forcing data. Application of the ensemble forcing in the CAM5 SCM during March 2000 intensive operational period (IOP) at the Southern Great Plains (SGP) of the Atmospheric Radiation Measurement (ARM) program shows systematic biases in the model simulations that cannot be explained by the uncertainty of large-scale forcing data, which points to the deficiencies of physical parameterizations. The SCM is shown to overestimate high clouds and underestimate low clouds. These biases are found to also exist in the global simulation of CAM5 when it is compared with satellite data.

1. Introduction

Large-Eddy Simulations (LES) [e.g. *Khairoutdinov and Kogan*, 2000; *Zhang et al.*, 2012], Cloud-Resolving Models (CRM)[e.g. *Khairoutdinov and Randall*, 2003; *Xu et al.*, 2002], and Single-Column Models (SCM) [e.g. *Del Genio et al.*, 2005; *Xie et al.*, 2002; *Xie et al.*, 2005] are important tools to develop and test physical parameterizations used in General Circulation Models (GCM) such as convections, turbulence, cloud microphysics and macrophysics. In these models, the large-scale dynamics are specified as the forcing terms to drive the physics. These forcing fields include vertical velocity and horizontal advective tendencies of temperature and moisture. To compare LES/CRM/SCM simulations with observations and to attribute model errors to deficiencies in physical parameterizations, accurate large-scale forcing data are needed.

Many objective analysis methods in the past have been carefully designed to derive large-scale forcing data from atmospheric sounding measurements [e.g. *Lin and Johnson*, 1996; *Ooyama*, 1987]. One widely used method is the constrained variational analysis algorithm (hereafter 1DCVA) developed by *Zhang and Lin* [1997]. Comparing to other conventional objective analysis methods, the unique feature of the 1DCVA is the use of surface and TOA observations as constraints to adjust atmospheric state variables from sounding measurements by the smallest possible amount to conserve column-integrated mass, moisture, dry static energy and momentum so that the final analysis data set is dynamically and thermodynamically consistent. This method has been used in the Atmospheric Radiation Measurement (ARM) program and several other field campaigns [*Schumacher et al.*, 2007; *Schumacher et al.*, 2008; *Xie et al.*, 2005; e.g. *Xie et al.*, 2006; *Xie et al.*, 2010a]. Recently, *Tang and Zhang* [2015] extended the 1DCVA algorithm

62 into a three-dimensional Constrained Variational Analysis (hereafter 3DCVA) at higher
63 horizontal resolutions and introduced additional features to improve the data quality. The
64 new 3DCVA derives large-scale forcing data in each grid of a certain domain
65 simultaneously, and all spatial grids are interacted with each other through advections.

66 This paper is a follow-up of *Tang and Zhang* [2015]. Because of the inevitable
67 uncertainties in the input data and objective algorithms, and because of the large
68 sensitivity of model results to the forcing data [*Hack and Pedretti*, 2000; *Hume and*
69 *Jakob*, 2005], it is necessary to quantify and understand the uncertainties in the derived
70 large-scale forcing data. The purpose of this paper is to introduce an ensemble approach
71 of 3DCVA and quantify the data uncertainties by analyzing the sensitivity of the forcing
72 data to the background data of the atmospheric state variables, the specification of the
73 error covariance matrix, and the constrained variables, which are required by 3DCVA.

74 The ensemble forcing data enable us to more confidently attribute errors in the
75 LES/CRM/SCM to physical sources when their simulated results are compared with
76 observations. We will show the applications of using the ensemble forcing data to
77 evaluate the simulated clouds in the Community Atmospheric Model (CAM5). Clouds
78 represent one of the largest uncertainties in current GCM simulations. Cloud simulations
79 are found to have large discrepancies from satellite- and ground- based observations.
80 *Zhang et al.* [2005] found that the majority of ten GCMs only simulated 30% to 40% of
81 the observed middle clouds and half of them underestimate low clouds comparing to
82 satellite cloud analysis from ISCCP (International Satellite Cloud Climatology Project)
83 and CERES (Cloud and the Earth's Radiant Energy System). *Xie et al.* [2005] evaluated
84 9 SCMs and 4 CRMs using ARM Baseline Microphysical Retrieval (MICROBASE)

85 ground measurements for a mid-latitude cyclone system, and found that the models
86 generally captured the bulk characteristics of frontal clouds but differed significantly in
87 the detailed structures. *Klein et al.* [2009] compared the simulations from 17 SCMs and
88 9 CRMs for an Arctic mixed phase cloud case. They found that the median simulated
89 liquid water path (LWP) is about one-third of the observed value, and the spread among
90 models are quite significant due to different physical schemes. *Jiang et al.* [2012]
91 examined 19 CMIP5 (Coupled Model Intercomparison Project phase 5) models and
92 found that both model-observation difference and model spread are large especially at the
93 upper troposphere levels. Although the model discrepancies are mainly attributed to
94 cloud parameterization errors other than to large-scale errors [e.g. *Su et al.*, 2013], it is
95 unclear how the physical parameterization and the large-scale atmospheric circulation
96 each contribute to the model errors. Moreover, the uncertainties of cloud retrievals from
97 different measurements and different retrieval algorithms are also large enough to affect
98 the evaluation of model results [*Huang et al.*, 2012; *Zhao et al.*, 2012]. With the
99 uncertainty of large-scale dynamics and observations specified, we can better attribute the
100 source of model biases.

101 The rest of the paper is organized as follows: Section 2 describes the method of
102 ensemble 3DCVA and data used in the method. Section 3 shows the ensemble mean
103 features of large-scale forcing data for one selected case and the sensitivities due to
104 different background data, error covariance matrix and constraint variables. Section 4
105 shows the sensitivities of SCM simulations due to large-scale forcing data and provides
106 an example of cloud bias evaluation and error source diagnosis. Summary and discussion
107 are given in Section 5.

2. Method, Data and Model

As described in *Tang and Zhang* [2015], the 3DCVA follows the general idea of 1DCVA [*Zhang and Lin*, 1997] that the atmospheric state variables (refers as background data hereafter) *u, v, q* and *s* are adjusted by minimizing the following cost function:

$$I=\left(u-u_o\right)^T B_u^{-1}\left(u-u_o\right)+\left(v-v_o\right)^T B_v^{-1}\left(v-v_o\right)+\left(q-q_o\right)^T B_q^{-1}\left(q-q_o\right)+\left(s-s_o\right)^T B_s^{-1}\left(s-s_o\right) \quad (1)$$

and satisfying the column-integrated conservation of mass, moisture and energy simultaneously across all spatial grids in the model domain:

$$\left\langle \nabla\cdot\vec{V}\right\rangle=-\frac{1}{g}\frac{dP_s}{dt} \quad (2)$$

$$\frac{\partial\langle q\rangle}{\partial t}+\left\langle \nabla\cdot\vec{V}q\right\rangle=E_s-P_{rec}-\frac{\partial\langle q_l\rangle}{\partial t} \quad (3)$$

$$\frac{\partial\langle s\rangle}{\partial t}+\left\langle \nabla\cdot\vec{V}s\right\rangle=R_{TOA}-R_{SRF}+L_vP_{rec}+SH+L_v\frac{\partial\langle q_l\rangle}{\partial t} \quad (4)$$

In addition, it adds the extra radiative constraints:

$$\frac{\partial s}{\partial t}+\nabla\cdot\left(\vec{V}s\right)+\frac{\partial\omega s}{\partial p}=Q_{rad} \quad (5)$$

at each level above observed cloud top (or a specified level when observed cloud top is low or absent) to physically reduce the spurious heating and cooling centers that are often seen near tropopause in both conventional objective analysis methods and 3DCVA. In the cost function Eq. (1), *u, v, q, s* are column vectors of horizontal winds, water vapor

mixing ratio and dry static energy ($s = C_p T + gz$, where C_p is heat capacity of air at constant pressure) for all grids in each time step. The superscript *T* denotes the transpose of a vector, the subscript *o* denotes the initial state, and *B* represents error covariance matrix for each state variable. In the constraint equations (2)-(5), the bracket represents vertical integration from the surface to the top of atmosphere (TOA), E_s is surface evaporation, P_{rec} is surface precipitation, L_v is the latent heat of vaporization, q_l is cloud liquid water content, R_{TOA} and R_{SRF} are net downward radiation at TOA and at surface, *SH* is surface sensible heat flux, ω is vertical velocity in pressure coordinate, and Q_{rad} is radiative heating rate calculated by the Rapid Radiative Transfer Model for GCMs. Other variables are as commonly used in meteorology.

The details of 3DCVA are described in *Tang and Zhang* [2015]. Here we highlight three sources of uncertainties (refers as elements hereafter) that impact the accuracy of 3DCVA results: background data, error covariance matrix and constraint variables. Background data are the first guess of the 3DCVA; all the adjustments are based on the original background data. Error covariance matrix, which is represented by *B* in Eq. (1), determines how the background data are adjusted spatially. Constraint variables, which are the right-hand-side terms of the constraint equations Eq. (2)-(5), control the budget of the whole system. Previous studies [*Xie et al.*, 2004; *Zhang et al.*, 2001] have shown that precipitation is the dominant constraint variables during rainy periods. In this study, we run 3DCVA using different combinations from six background data, five error covariance matrices and three precipitation estimates (Table 1, details described below) to analyze the uncertainties in the derived forcing fields.

Background data	RUC, ERA-interim, CFSR, JRA55, MERRA, NARR (details see Table 2)
Error covariance matrix	Calculated from variance of time series, only auto correlation.
	Calculated from variance of ensemble members, only auto correlation.
	Calculated from variance of ensemble members, vertical correlation.
	Calculated from variance of ensemble members, horizontal correlation.
	Calculated from variance of ensemble members, horizontal and vertical correlation.
Constraint variables	Arkansas-Red Basin River Forecast Center (ABRFC) gridded precipitation products
	Upper bound: 1.4 × ABRFC precip amount
	Lower bound: 0.6 × ABRFC precip amount

148 Table 1: different background data, error covariance matrix and constraint variables used in
149 ensemble 3DCVA.

150

Name	Data Assimilation	Assimilation Intervals	Model Resolution	Model Vertical levels
ERA-interim *Dee et al.*, 2011	4DVAR	12 hour	T255 (79km×79km)	60
CFSR *Saha et al.*, 2010	3DVAR with flow dependence error variance	6 hour	T382 (38km×38km)	64
MERRA *Rienecker et al.*, 2011	3DVAR with incremental analysis update (IAU)	6 hour	1/2° × 2/3°	72
JRA55 *Kobayashi et al.*, 2015	4DVAR	6 hour	TL319 (55km×55km)	60
NARR *Mesinger et al.*, 2006	3DVAR with precipitation assimilated	3 hour	32km×32km	45
RUC *Benjamin et al.*, 2004	3DVAR	1 hour	40km×40km	40

151 Table 2: the six background data used in the ensemble 3DCVA. All datasets are interpolated into
152 0.5°×0.5° horizontal resolution, 27 vertical levels from 1000hPa to 100hPa and 3-hourly time
153 resolution.

154

155 The six background data are obtained from reanalysis/analysis products listed in
156 Table 2. They are linearly interpolated into 0.5°×0.5° horizontal resolution, 3-hourly
157 time resolution and 27 vertical levels from 1000 hPa to 100 hPa. Most of the constraint
158 variables are derived from ARM surface station measurements, which include the
159 following datasets:

160 • Surface Meteorological Observation Stations (SMOS) measuring precipitation,
161 pressure, winds, temperature, and relative humidity at the surface.
162 • Energy Budget Bowen Ratio (EBBR) stations measuring surface latent and
163 sensible heat fluxes and surface broadband net radiative flux.
164 • Eddy Correlation Flux Measurement System (ECOR) providing in situ half-hour
165 averages of the surface vertical fluxes of momentum, sensible heat flux, and latent
166 heat flux.
167 • Oklahoma and Kansas mesonet stations (OKM and KAM) measuring surface
168 precipitation, pressure, winds, and temperature.
169 • Microwave Radiometer (MWR) stations measuring the column precipitable water
170 and total cloud liquid water.

171 These surface measurements are interpolated into 0.5°×0.5° horizontal resolution
172 covering the SGP domain. If there are actual measurements within the 0.5°×0.5° grid
173 box, simple arithmetic averaging is used to obtain the value for that grid box. Under
174 circumstances that multiple instruments observe the same quantities, their measurements
175 are merged in the arithmetic averaging process with a weighting function depending on
176 their quality. If there is no actual measurement in the grid box, the Barnes scheme
177 [*Barnes*, 1964] is used with the length scale of L_x=50km, L_y=50km, and L_t=6hr to fill the

178 missing grid box. The satellite measurements of radiative fluxes and cloud top pressure
179 are available at NASA Langley [*Minnis et al.*, 2008] measured by the Geostationary
180 Operational Environment Satellite 8 (GOES8) in 0.5°×0.5° grid box. The precipitation
181 rate data is obtained from the 4-km resolution gridded precipitation products from
182 Arkansas-Red Basin River Forecast Center (ABRFC) based on WSD-88 rain radar and
183 gauge measurements, and is averaged into 0.5°×0.5° horizontal resolution and 3-hourly
184 time resolution. The spatial distribution of the surface and TOA measurements used in
185 this study are shown in Figure 1.

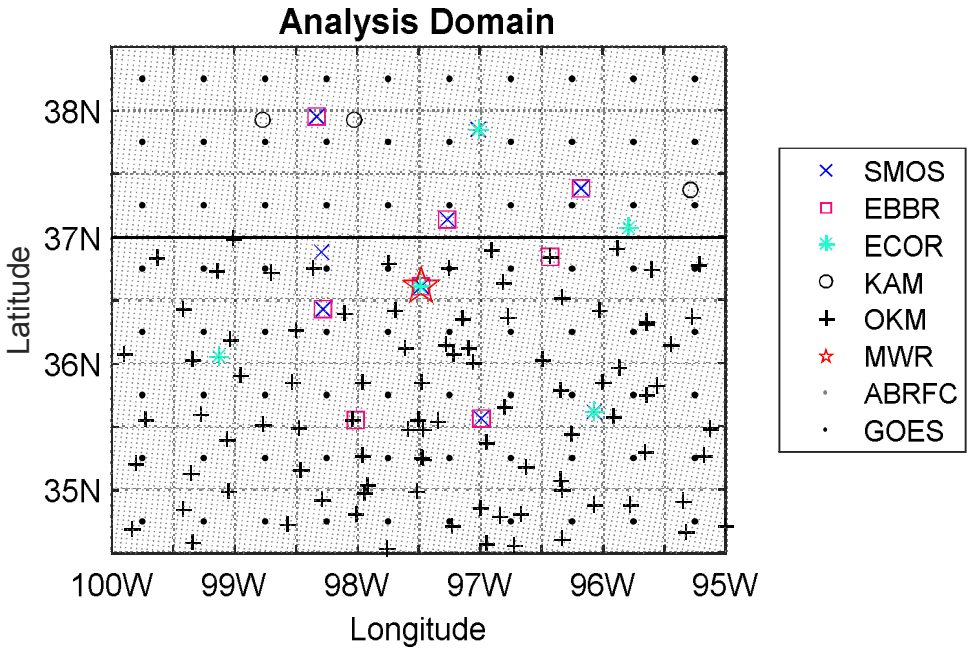

186

187 Figure 1: Analyzed SGP domain and surface/TOA observations. Different marks show different
188 instruments. Gray lines show 0.5°× 0.5° grids in 3DCVA which are the same as grids of GOES
189 satellite products (black dots). Black line at 37°N indicates the boundary between Oklahoma
190 (below) and Kansas (above).

191

192 Surface and TOA measurements of constraint variables contain errors from
193 instrument uncertainties, assumptions and limitations in the retrieval algorithms, and

194 interpolation from stations to regular grids. As shown in *Xie et al.* [2004], precipitation is
195 the most dominant constraint during precipitation periods. In this study, we will focus on
196 the impact of precipitation uncertainties on the derived large-scale forcing data.
197 Following *Xie et al.* [2014], we consider a 40% fractional root-mean-square error (RMSE)
198 for ABRFC rainfall products, and use the estimated rain rate, the upper bound (1.4 times
199 estimated rain rate), and the lower bound (0.6 times estimated rain rate) of the uncertainty
200 to form the ensemble members. The 40% uncertainty is only considered on the
201 magnitude of the rain rate.

202 We have two methods to calculate the error covariance matrix. One method is the
203 original algorithm [*Zhang and Lin*, 1997; *Zhang et al.*, 2001] in 1DCVA, which
204 calculates the covariance from the variance of time series of the background data plus
205 instrument and measurement uncertainties with no correlation. The other method is
206 described in *Tang and Zhang* [2015] which calculates the covariance by using the
207 anomaly of different background data relative to their ensemble mean. In this method,
208 we can have the different correlation types of no correlation, vertical correlation only,
209 horizontal correlation only, and both horizontal and vertical correlations in which
210 adjustments of each grid point will have different correlations to its surrounding grids and
211 levels. In total we can have five error covariance matrices to run the ensemble 3DCVA.
212 Combining 6 background fields, 3 precipitation rates (representing constraint variables),
213 and 5 covariance matrices, we therefore have a total of 90 3DCVA ensemble members.

214 A SCM version of CAM5 (SCAM5) is used to test the impact of uncertainties in
215 the large-scale forcing data. CAM5 is the latest version of the NSF/DOE Community
216 Atmospheric Model developed at the Nation Center for Atmospheric Research (NCAR),

217 which contains a range of significant enhancements in the representation of moist
218 physical processes relative to its predecessors [*Neale et al.*, 2012]. These include: (1) a
219 turbulent kinetic energy (TKE) based boundary layer scheme that can explicitly simulate
220 stratus-radiation-boundary layer interactions [*Bretherton and Park*, 2009]; (2) a new
221 shallow convection scheme combined with the above boundary layer scheme [*Park and*
222 *Bretherton*, 2009]; and (3) a new bulk two-moment cloud microphysics scheme for
223 stratiform-clouds [*Morrison and Gettelman*, 2008] that predicts both mixing ratios and
224 number concentrations of cloud droplets (liquid) and crystals (ice). CAM5 is part of the
225 Community Earth System Model (CESM) that has been used in Phase 5 of the Coupled
226 Model Intercomparison Project (CMIP5).

227 The observed cloud properties used to evaluate the SCAM5 simulations are
228 obtained from ARM Baseline Microphysical Retrieval (MICROBASE) which is a cloud
229 retrieval product combining multiple measurements from cloud radar, lidar, ceilometer,
230 microwave radiometer and soundings. Other variables such as liquid water path (LWP)
231 and radiative fluxes are obtained from ARM Best Estimate (ARMBE) products [*Xie et al.*,
232 2010b] at SGP central facility. We average these data into 3-hour intervals in order to
233 compare with SCAM5 simulations.

234 The satellite retrievals used to evaluate the CAM5 GCM results is the merged
235 CALIPSO, CloudSat, CERES, and MODIS product C3M [*Kato et al.*, 2011]. It has
236 global coverage from July 2006 to June 2010 for 4 years. Cloud fraction in this product
237 is obtained from CALIPSO data with CloudSat clouds assigned into CALIPSO bins.
238 Liquid water content (LWC) and ice water content (IWC) are derived from the radar-only
239 algorithm from CloudSat and normalized by LWP from MODIS measurements.

240

241 **3. Ensemble Constrained Variational Analysis of Large-Scale Forcing Data**

242 3.1 Ensemble mean

243 The ARM March 2000 Intensive Operational Period (IOP) at the Southern Great
244 Plains (SGP) is used in this study. This IOP contains several precipitation events with
245 various types of clouds, which has been extensively examined in earlier process studies
246 [e.g. *Xie et al.*, 2005; *Xu et al.*, 2005]. The 3D structure of a mid-latitude cyclone case on
247 3 March has been analyzed by *Tang and Zhang* [2015]. Here we emphasize the SGP
248 domain averaged large-scale forcing data during the whole IOP. The SGP domain in this
249 study is following the domain used in *Tang and Zhang* [2015], which is a rectangle
250 domain from 34.5-39°N, 95-100°W, with 0.5°×0.5° horizontal resolution shown in
251 Figure 1.

252 Figure 2 shows the domain averaged ensemble mean analyzed *u, v, q, s* from the
253 ensemble 3DCVA, and the domain averaged ensemble mean adjustments for each
254 variable. The domain mean adjustments of horizontal winds are smaller than 0.5 m s^{-1},
255 but the standard deviation of adjustments on horizontal grids (not shown) are in the
256 magnitude of 1 m s^{-1}, indicating that the winds adjustments have compensatory effects
257 horizontally, which brings large change to the divergence and advections. The average
258 adjustment of q is generally smaller than 0.5 g kg^{-1}, except for one low-level point at 18Z
259 on 4 March. Adjustments of s have a diurnal cycle with warm adjustments of ~0.3K in
260 the daytime and cold adjustments of ~0.1K in the nighttime. The periodic feature of s
261 adjustments indicates the inconsistency of diurnal cycle in the background data and in the

column energy budget, which may due to the unrealistic simulations of diurnal cycle in reanalysis/analysis models. The domain averaged adjustment of q and s has a similar magnitude to the standard deviation of adjustments on horizontal grids (not shown).

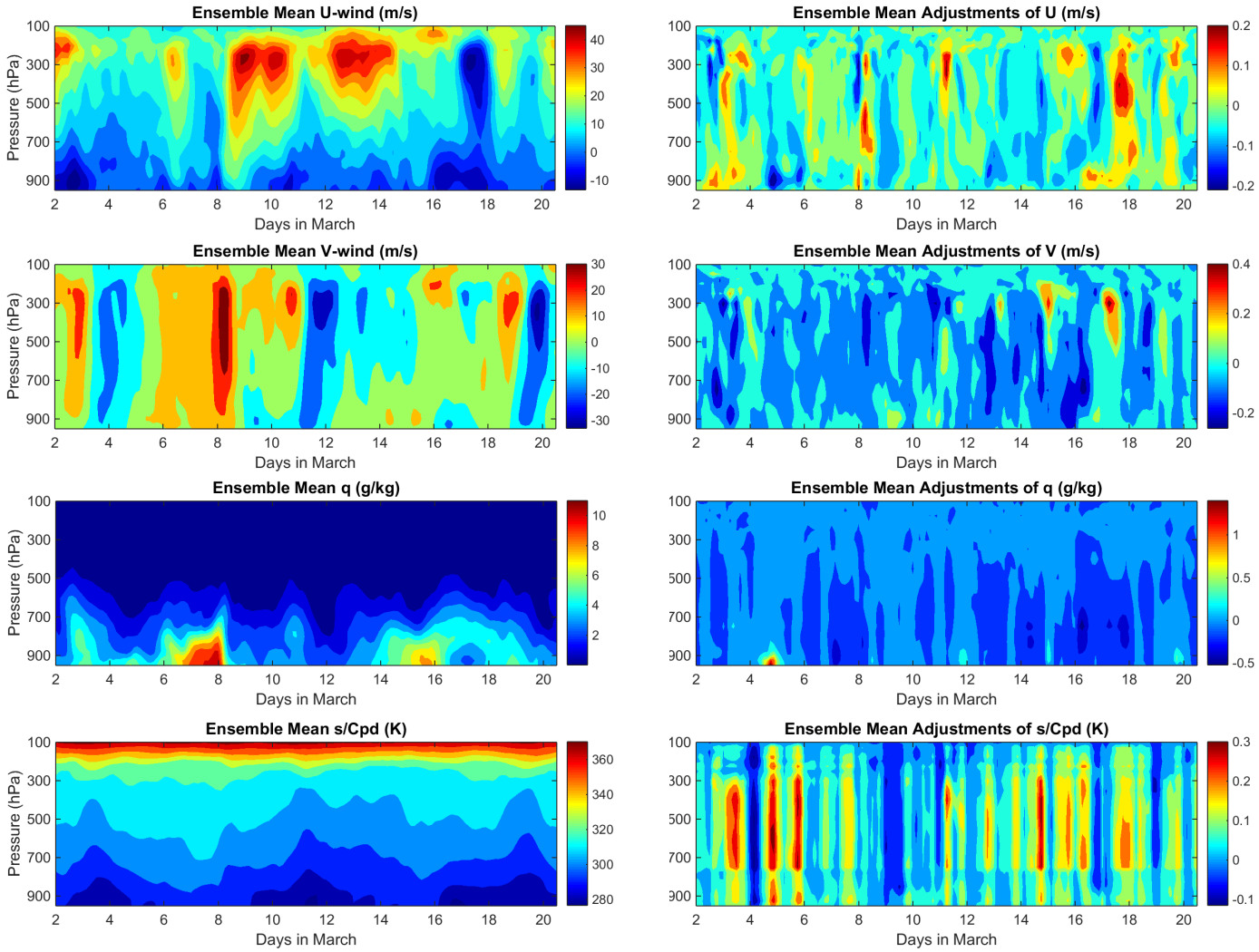

Figure 2: (left) SGP domain averaged ensemble mean horizontal winds, moisture and dry static energy (u, v, q, s) and (right) SGP domain averaged adjustments of u, v, q, s.

Figure 3 shows the domain averaged precipitation and ensemble mean temperature, moisture, vertical velocity (omega), as well as horizontal and vertical advections of q and s, which are key variables of the large-scale forcing data. The precipitation occurs on 2-3 March, 8 March, 11March, and 16-19 March, separately. The rising motion and advections of q and s correspond well with these events. The general patterns are also consistent with forcing data derived from 1DCVA (not shown), which uses the same source of constraint variables within a slightly smaller domain at SGP. In the next section, we will discuss the impact of the three elements of ensemble 3DCVA on the analyzed large-scale forcing data.

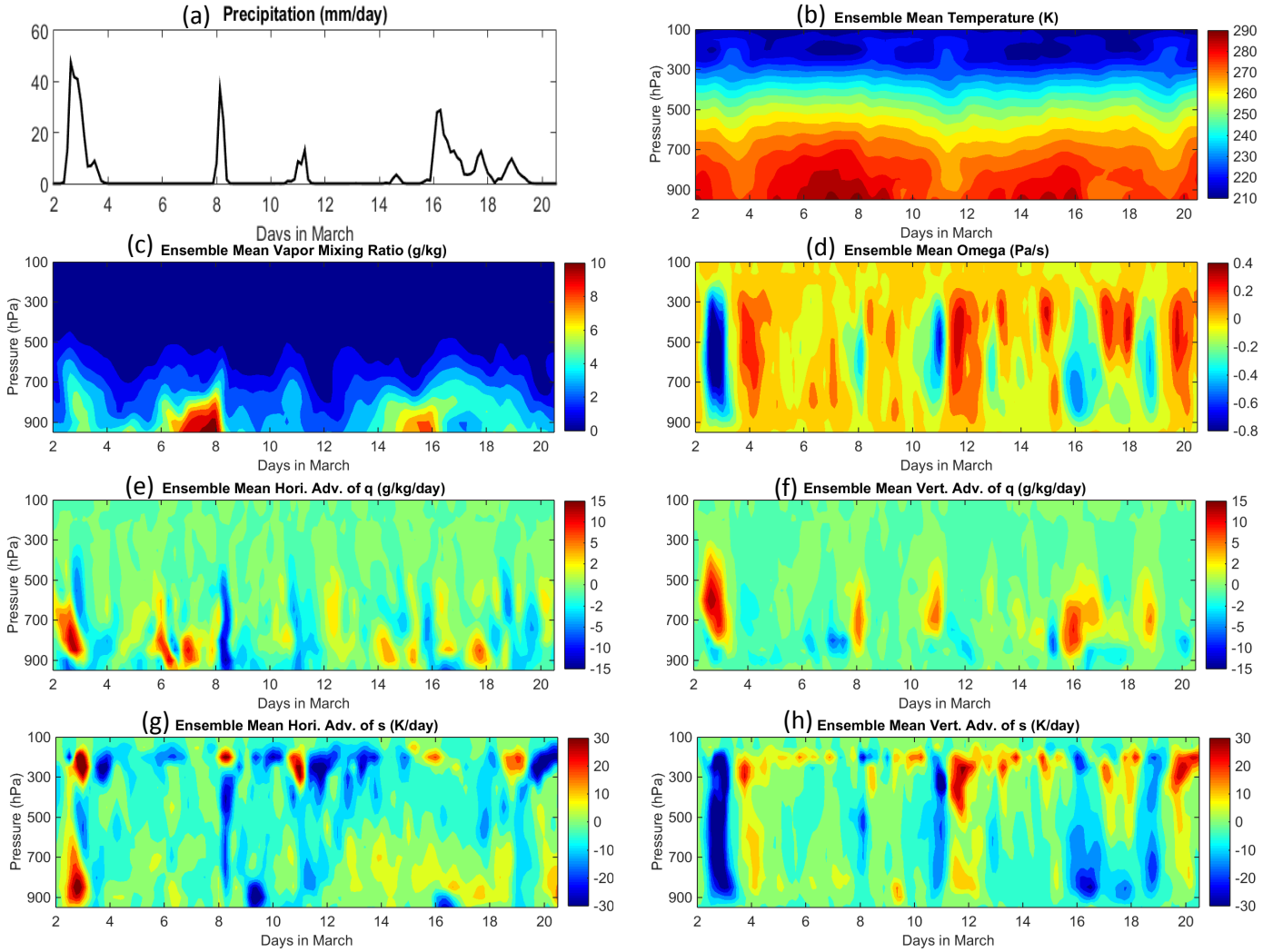

279 Figure 3: (a) SGP domain averaged precipitation and domain averaged ensemble mean profiles of
280 (b) temperature, (c) water vapor mixing ratio, (d) vertical velocity, (e – h) horizontal and vertical
281 advections of q and s.

282

283 3.2 Analysis of sensitivity and uncertainty

284 To understand the sensitivities of large-scale forcing data to different elements in
285 3DCVA, we calculated the standard deviations of large-scale forcing data due to different
286 background data, error covariance matrices and precipitation rates (Figure 4). For each
287 one element (such as background data), we average the large-scale forcing data over the
288 other two elements (such as error covariance matrix and precipitation rate). The
289 magnitude of standard deviation of temperature and water vapor mixing ratio is generally
290 smaller than 2K and 1g kg^{-1}, respectively; the magnitude of vertical velocity and
291 advective tendencies of q and s are around 0.2Pa s^{-1}, 5g kg^{-1} day^{-1}, and 10K day^{-1},
292 respectively. The relative uncertainties of vertical velocity and advective tendencies are
293 much larger than the relative uncertainties of temperature and moisture. The standard
294 deviation due to different background data is larger than that due to error covariance and
295 precipitation in most of time, indicating the importance of the initial first guess to the
296 final forcing data. For uncertainties due to precipitation, horizontal moisture advection
297 has much larger uncertainty than other variables, which indicates tight relationship
298 between the horizontal moisture advection and precipitation process.

299

300

301

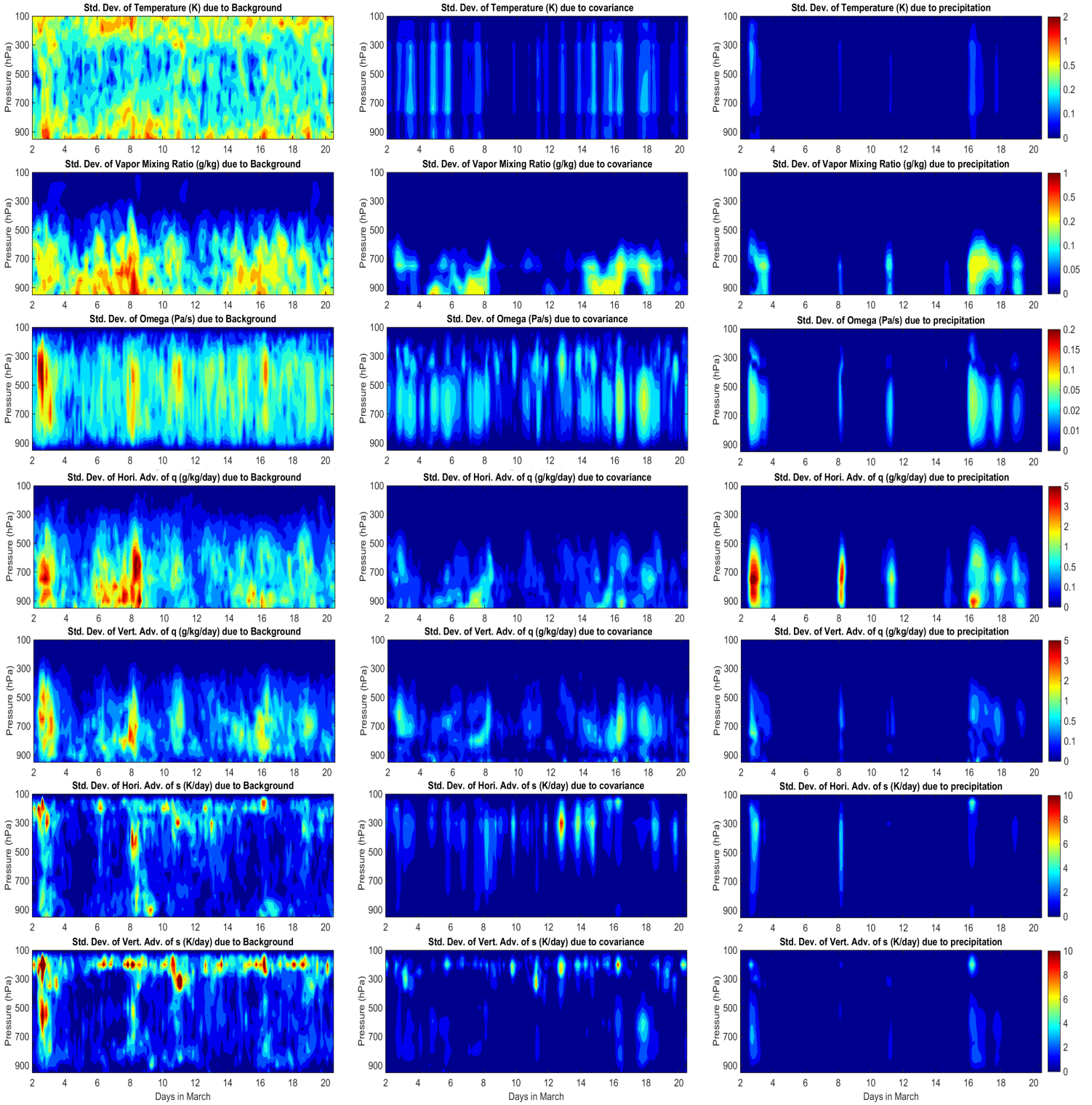

Figure 4: the standard deviations of large-scale forcing data (from top to bottom: T, q, ω, horizontal and vertical advections of q and s) to different background data (left), error covariance matrices (middle) and precipitation rates (right).

306 To investigate the overall uncertainties of large-scale forcing data due to all the
307 three elements, we define the relative 1-sigma uncertainty as the standard deviation of the
308 90 ensemble members divided by the temporal standard deviation of the ensemble mean
309 fields. As shown in Table 3, during the whole IOP, the domain mean 1-sigma uncertainty
310 is about 1.5% for temperature and 5.6% for vapor mixing ratio. If we separate it into
311 precipitation periods and non-precipitation periods, the 1-sigma uncertainty in
312 temperature (water vapor mixing ratio) is 1.6% (6.3%) for precipitation periods and 1.4%
313 (4.9%) for non-precipitation periods. For the analyzed forcing fields, the mean 1-sigma
314 uncertainty in vertical velocity and advective tendencies of q and s is 21.6%, 24.9% and
315 27.0% for the whole IOP, 26.7%, 32.5% and 31.9% for precipitation periods, and 16.7%,
316 17.6% and 22.4% for non-precipitation periods, respectively. It is clear that these large-
317 scale forcing data are more uncertain during precipitation periods than during non-
318 precipitation period.

319

	Temperature	**Water Vapor Mixing Ratio**	**Vertical Velocity**	**Advections of *q***	**Advections of *s***
Whole IOP	1.5%	5.6%	21.6%	24.9%	27.0%
Precip	1.6%	6.3%	26.7%	32.5%	31.9%
Non-precip	1.4%	4.9%	16.7%	17.6%	22.4%

320

321 Table 3: The 1-sigma uncertainties of large-scale forcing data due to all different elements. For
322 advections of q and advections of s, the uncertainty is the average of the uncertainties of
323 horizontal and vertical advections.

The vertical profiles of these large-scale forcing data averaged over the precipitation period and non-precipitation period and their standard deviations are shown in Figure 5. There are significant differences between vertical profiles of the precipitation period and non-precipitation period. During the precipitation period, it has lower temperature and higher moisture at lower level. The vertical velocity shows rising motion throughout the whole troposphere during the precipitation period while sinking motion during the non-precipitation period, which contributes to opposite signs in vertical advections of q and s. Advections of s at upper-levels have larger sensitivities than at mid- and low-levels, which may be related to the relatively larger gradient of s at the tropopause.

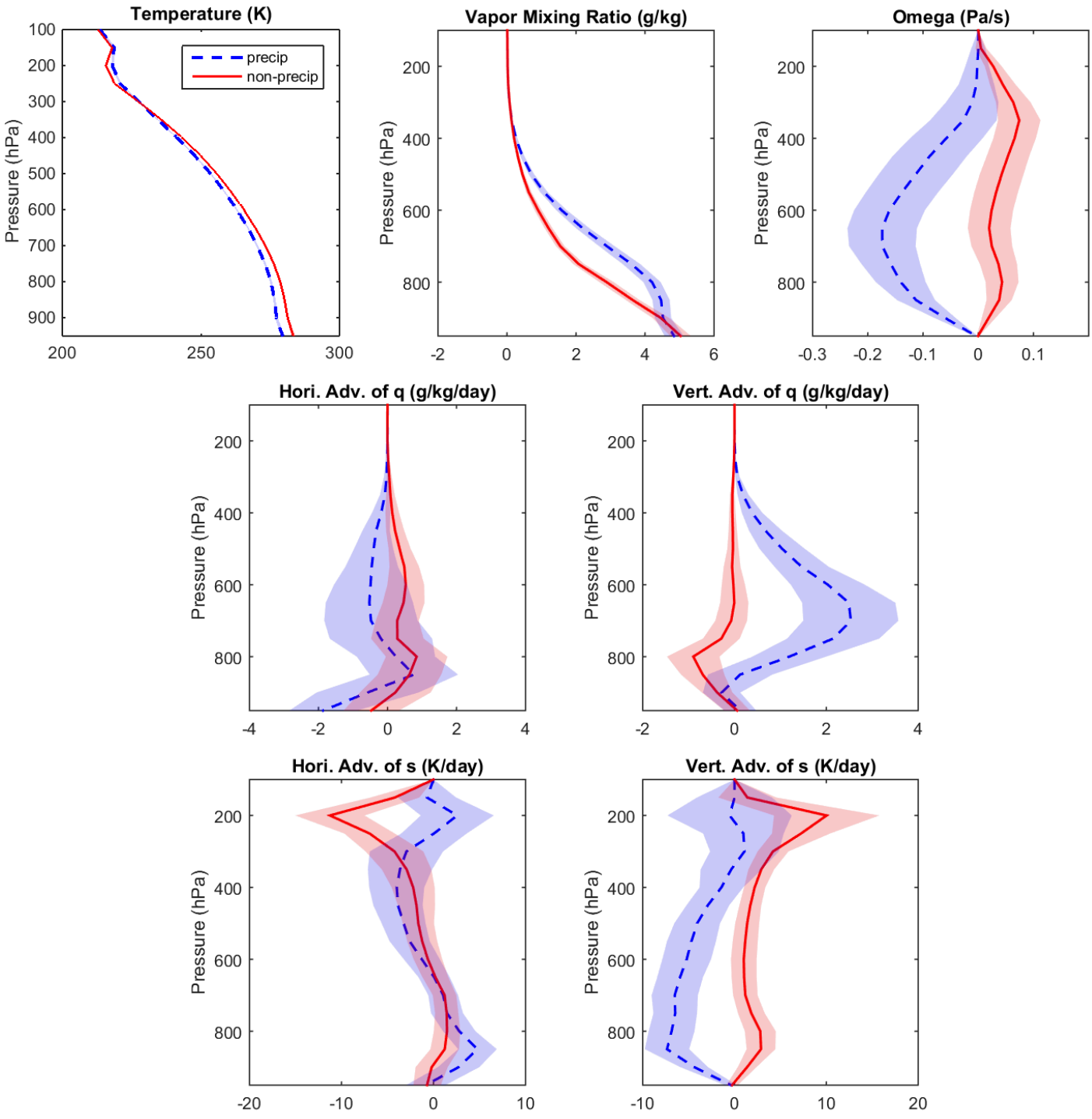

335

336 Figure 5: Ensemble mean vertical profiles of (up): temperature, vapor mixing ratio, vertical
337 velocity, (middle): horizontal and vertical advection of q and (bottom): horizontal and vertical
338 advection of s averaged for precipitation period (blue) and non-precipitation period (red). The
339 time-mean standard deviations are shown in shade.

340

341 **4. Application of Ensemble Forcing Data on Evaluating Cloud Bias in CAM5**

342 4.1 Sensitivity of SCM simulations

343 We next analyze the sensitivity of SCM simulations to different elements in the
344 large-scale forcing data. Here we run SCAM5 using each member of the ensemble large-
345 scale forcing data (SGP domain mean), restarting at 15Z every day from 1 March to 19
346 March for 36 hours without relaxation, and choose the hour 9 to 33 of the simulations
347 (00Z to 24Z of the next day) to test the sensitivities of model results to different
348 background data, error covariance matrices and constraint variables. Surface sensible
349 and latent heat fluxes are prescribed from the forcing data.

350 The time-pressure cross sections of the ensemble mean simulated cloud fraction,
351 liquid water content (LWC) and ice water content (IWC) are shown in Figure 6 (left).
352 Also shown in the figure are the observations obtained from MICROBASE during this
353 period (right). Note that the model IWC in this study includes both cloud ice and snow
354 since observation does not separate the two. The models captured most of the major
355 cloud events during the IOP, with good consistency to observations especially in the
356 cloud fraction.

357

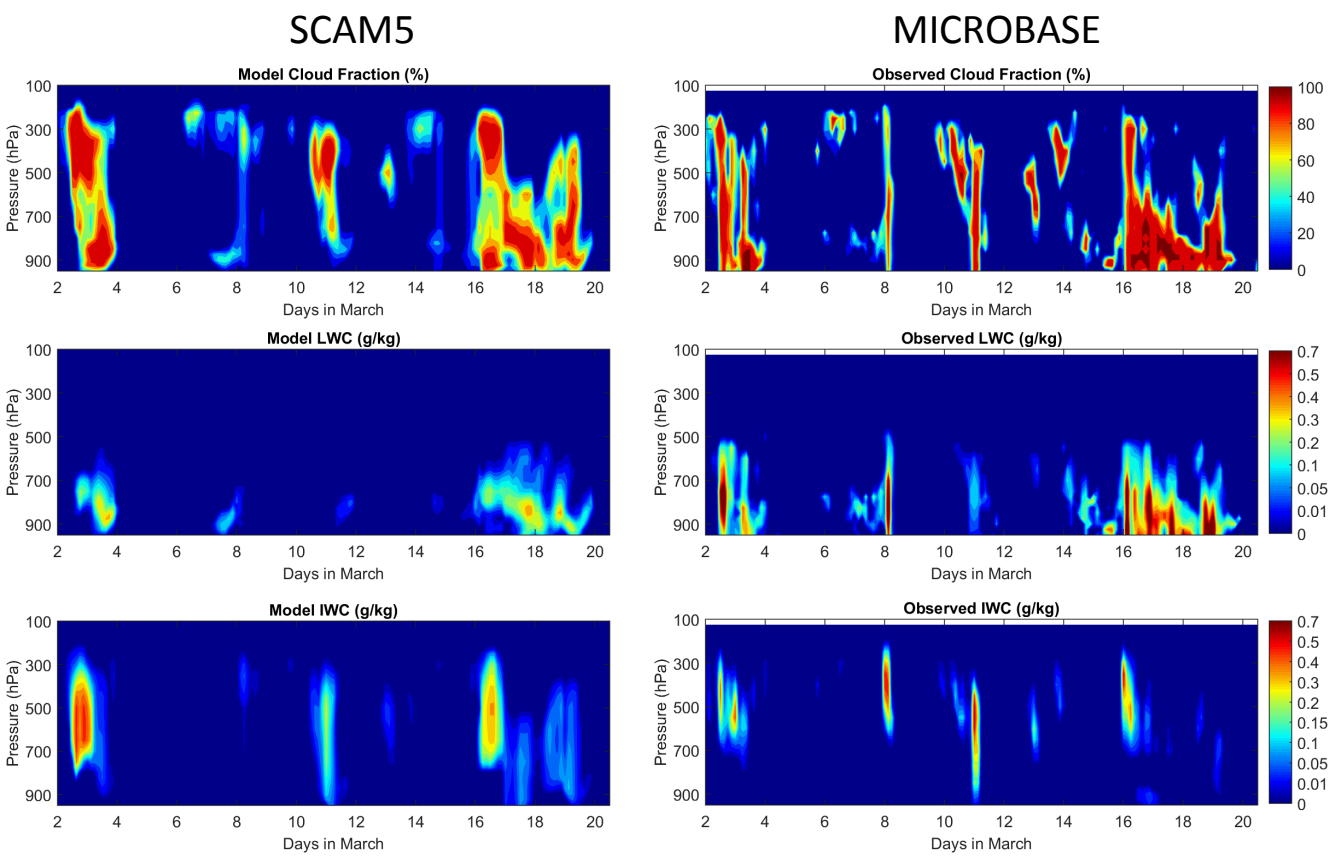

Figure 6: the ensemble average of SCAM5 (left) simulated cloud properties and cloud retrievals from MICROBASE (right). From top to bottom: cloud fraction, LWC and IWC (model IWC includes both cloud ice and snow).

The standard deviations of simulated cloud fraction, LWC and IWC to different elements of large-scale forcing data are shown in Figure 7. The uncertainty of cloud properties at some time steps could reach up to more than 50% of simulated values, implying that the amount of the cloud fraction and hydrometeors is sensitive to the initialization of large-scale forcing data. The mean 1-sigma uncertainty is about 25.9% for cloud fraction, 17.6% for LWC and 16.1% for IWC. Among the three elements in 3DCVA, background data are the largest contributor to uncertainties of cloud fraction and LWC, which is similar to the results in the previous section. However, IWC is more

371 sensitive to the precipitation rather than to the background data. Further analysis shows
372 that the cloud ice is more sensitive to the background data, but snow, which is much
373 larger than cloud ice mixing ratio, is more sensitive to the precipitation. Overall,
374 different elements in the large-scale forcing data have considerable impacts on SCM
375 cloud simulation.

376

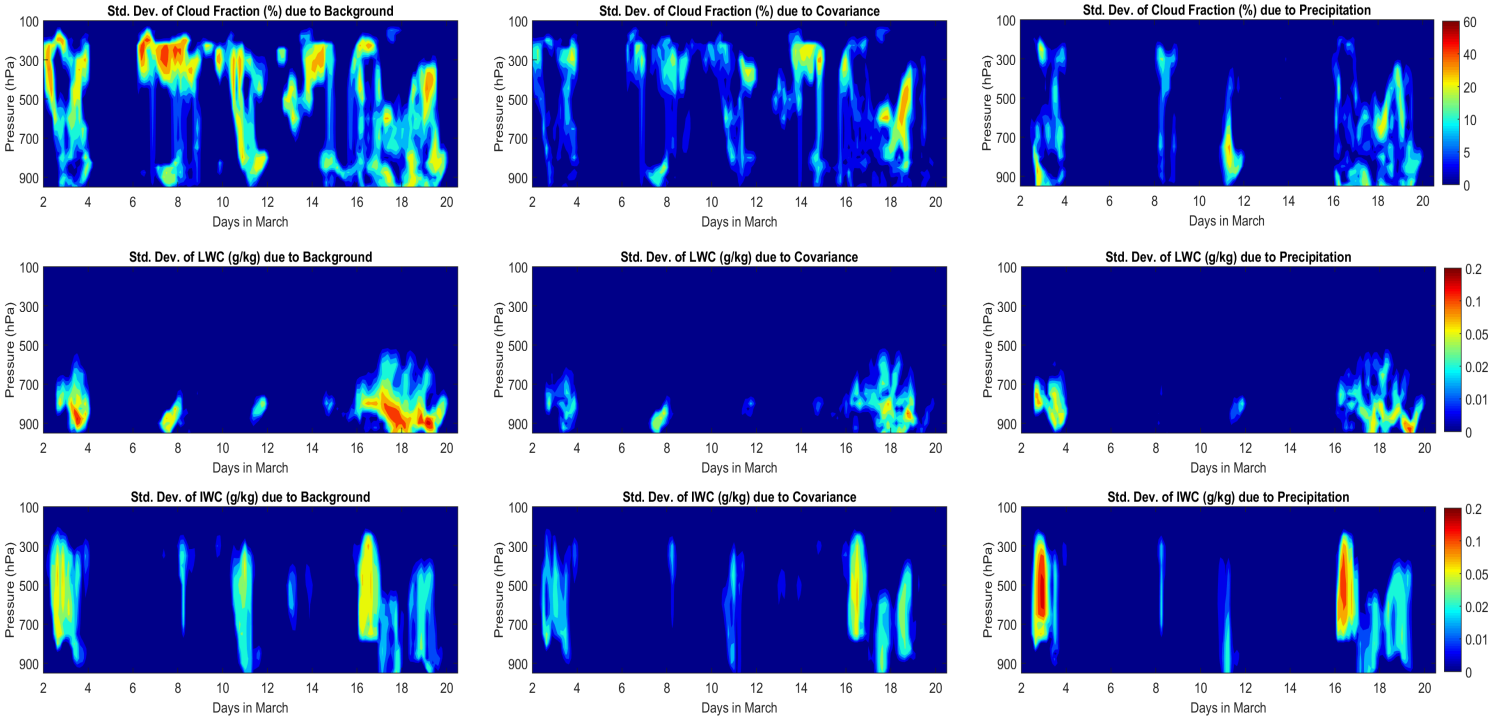

377

378 Figure 7: the standard deviations of SCAM5 simulated clouds (from top to bottom: cloud fraction,
379 LWC and IWC) due to different background data (left), error covariance matrices (middle) and
380 precipitation (right).

381

382 4.2 Evaluation of model biases using ensemble simulations

383 In SCMs, model errors come from two sources: deficiencies in physical
384 parameterizations and uncertainties in large-scale forcing data. By considering

uncertainties in both large-scale forcing data and observed validation data, we can better identify the source of model bias (discrepancy between models and observations): whether the model bias can be explained by the uncertainties in forcing data and observed validation data, or if it comes from physical parameterizations (true model errors).

In this study, the model uncertainties due to large-scale forcing data are estimated as twice of the model standard deviation (2-sigma uncertainty) using different large-scale forcing data from all 90 3DCVA members listed in Table 1. The uncertainties in the MICROBASE cloud retrievals are estimated as 15% for LWC, 55% for IWC and 25% for cloud fraction. These numbers are based on the study by *Zhao et al.* [2014] in which they perturbed key inputs and parameters in cloud retrieval algorithms and estimated these uncertainties. Limitations and caveats about the cloud retrievals will be discussed later.

Figure 8 shows the model bias of cloud fraction, LWC and IWC in time-pressure profiles (right), and the vertical profiles averaged in the whole period (left). The black lines in the right panel highlight regions where model biases are larger than the uncertainties from forcing data and observations:

$$\left|\text{SCAM5} - \text{MICROBASE}\right| > \sqrt{\left(2\sigma_{forcing}\right)^2 + \sigma_{obs}^2} \qquad (6)$$

where $\sigma_{forcing}$ is the 1-sigma uncertainty of SCAM5 simulations due to different forcing data, and σ_{obs} is the observation uncertainty specified above. It is seen that SCAM5 overestimates high-cloud while underestimates low-cloud, consistent with its overestimation of IWC and underestimation of LWC. Most of these biases are

406 significantly larger than the total uncertainties from large-scale forcing data and
407 observations, indicating that these biases are due to the deficiencies of physical
408 parameterizations in the model. For IWC, most of the model overestimation is within the
409 uncertainties from large-scale forcing data and observations.

410

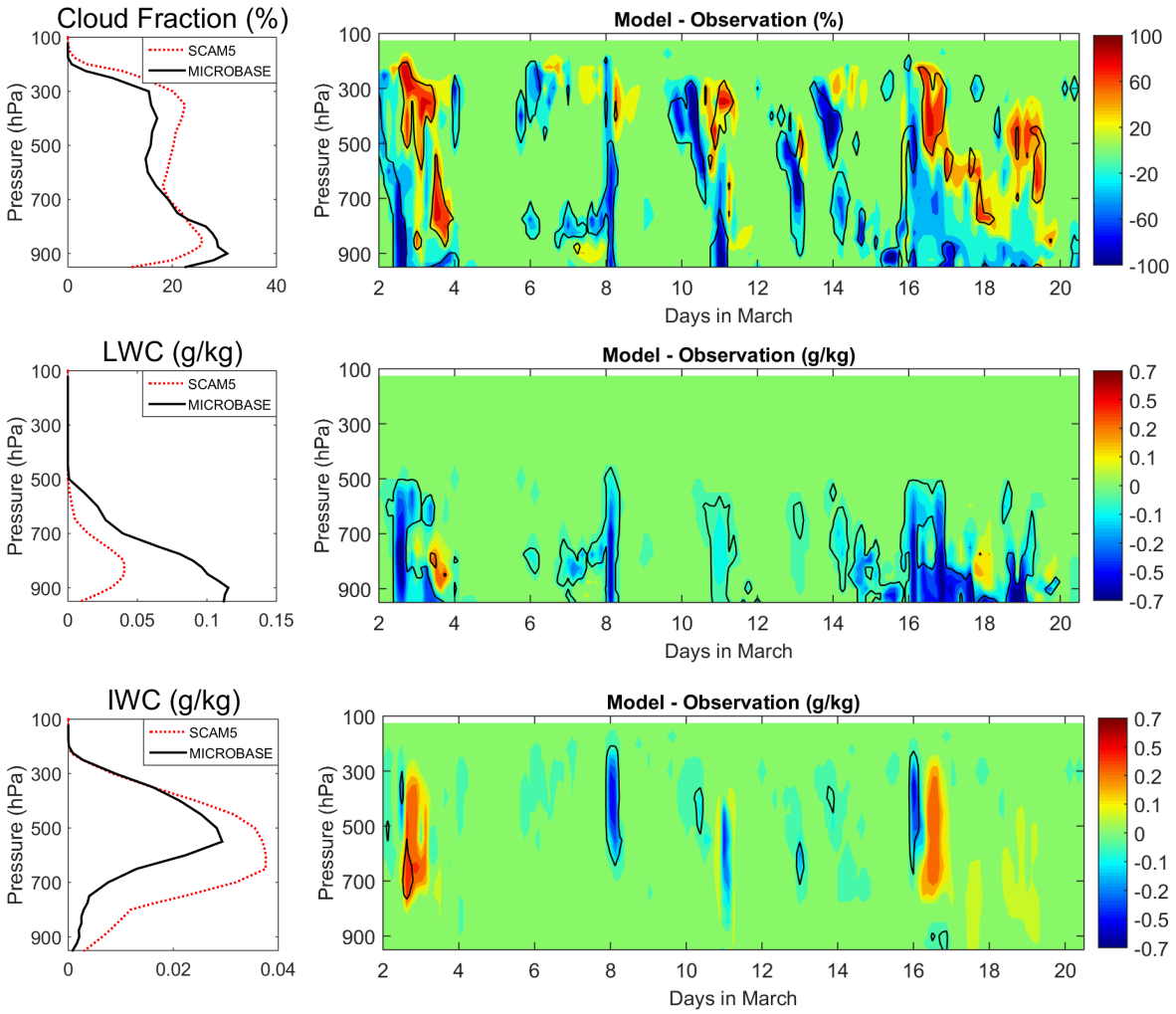

411

412 Figure 8: (right) SCAM5 model bias of cloud properties. Blue color means model
413 underestimation while yellow/red means overestimation, with black lines circle out where model
414 bias is larger than the total uncertainties from large-scale forcing data and observations. (left)
415 vertical profiles averaged during the whole period. Black line is MICROBASE, red dashed line
416 is SCAM5. From top to bottom: cloud fraction, LWC and IWC (IWC includes both cloud ice and
417 snow).

418

419 The uncertainties of the cloud hydrometeor retrievals given above could be
420 underestimated. *Zhao et al.* [2014] pointed out that when considering all assumptions
421 and for precipitating clouds, uncertainties could be larger than those given in this study.
422 The spread among different products may be much larger than the diagnosed
423 uncertainties [*Zhao et al.*, 2012]. Later analysis will also show this large spread (Figure
424 10). *Huang et al.* [2012] suggests that different input data, different treatments of rain
425 contamination and mixed-phase clouds are mainly responsible for the large differences of
426 retrieved LWC.

427 Given the large uncertainties in the cloud retrievals, it is important to examine if
428 model errors shown in cloud properties are consistent with those exhibited in other
429 relevant fields. Figure 9 compares the LWP, outgoing long wave flux at TOA, total cloud
430 fraction (daytime mean) and surface downward shortwave flux (daily mean) between the
431 observations (ARMBE) and SCAM5 simulations. The standard deviations of model
432 simulations due to different forcing data are shown in the shaded area. The use of daily
433 averaging for the surface downward shortwave flux is to remove the strong diurnal cycle
434 and the use of daytime averaging for the total cloud fraction is to make it consistent with
435 surface downward shortwave flux because there is no shortwave flux at nighttime. The
436 time variations of these variables are overall consistent with cloud fraction and
437 hydrometeors during this period.

438

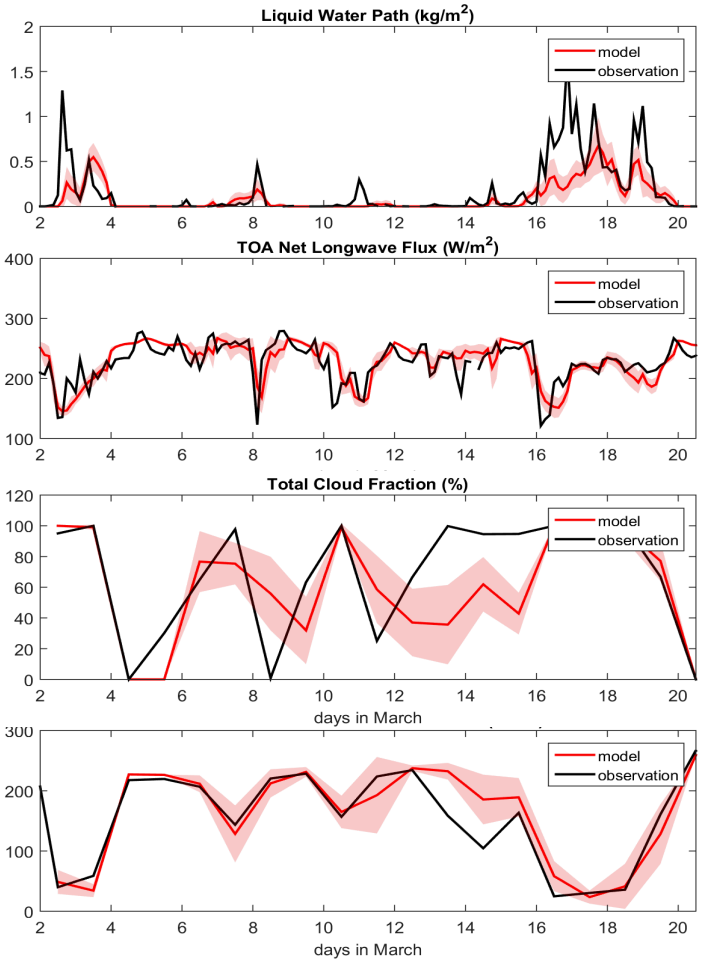

439

440 Figure 9: Ensemble mean SCAM5 simulations (red line) with standard deviations due to different
441 large-scale forcing data (red shade) and observations from ARMBE (black). From up to bottom:
442 LWP, TOA net longwave flux, total cloud fraction (daytime mean) and surface downward
443 shortwave flux (daily mean).

444

445 It can be seen that the LWP in SCAM5 is lower than the observed value during
446 most of cloud/precipitation events. The simulated LWP (with standard deviation, same
447 as below) averaged during the whole IOP is 94.8±6.9 g m^{-2}, comparing to the observed
448 191.3 g m^{-2}. Note that LWC in MICROBASE has been constrained by the LWP at the
449 SGP central facility so the LWC and LWP are not independent. We therefore examine

450 the radiation fields at the TOA and surface, which are independent with the retrieved
451 cloud properties.

452 For longwave flux at TOA, SCAM5 missed some cloud events on 10 and 14
453 March, where longwave flux has a sharp decrease in the observations but is relatively flat
454 in the model. During the whole IOP, SCAM5 has TOA longwave flux of 229.4±1.1 W
455 m^{-2}, slightly larger than the observed 227.6 W m^{-2}. However, the model does not always
456 overestimate longwave flux at TOA. During times when SCAM5 has more high cloud
457 fraction than observations in Figure 8, it also underestimates longwave flux (on 3, 17
458 and19 March).

459 For total cloud fraction and surface downward shortwave flux, daily (daytime)
460 averaging is used to smooth out some short-period cloud features. From 13 to 15 March,
461 the model overestimation of surface downward shortwave fluxes is consistent with the
462 underestimation of total cloud fraction. These consistencies between the biases of cloud
463 properties with biases of radiation fluxes give us more confidence in attributing model
464 biases to the deficiencies of physical parameterizations.

465 4.3 Applicability of SCM results to GCM

466 The above analysis of model biases is limited to one single IOP. To understand
467 the applicability of the SCM results in this IOP to the GCMs climatologically and
468 globally, we compare the simulations of clouds in the global CAM5 with satellite cloud
469 retrievals C3M to examine if the biases in SCAM5 still exist in CAM5 GCM.

470 Figure 10 shows the climatological mean cloud fraction, LWC and IWC at SGP
471 site (or the nearest grid) from CAM5 (blue), C3M (red) and MICROBASE (black),

472 respectively. For cloud fraction, both the C3M and MICROBASE data show that CAM5
473 overestimates high clouds and underestimates low clouds, which is consistent with
474 SCAM5 results discussed earlier. For LWC, the differences between the two
475 observations are too larger to draw a firm conclusion about the CAM5 GCM (note that
476 the x axis is in logarithm scale). The reason of large LWC differences between C3M and
477 MICROBASE remains unclear. One possible cause is the different assumptions used in
478 the retrieval algorithms, where C3M assumes all clouds are liquid (ice) phase when
479 retrieving LWC (IWC), while MICROBASE assumes cloud droplets number
480 concentration is constant (100 cm^{-3}). The different angles of measurements could be
481 another reason, where C3M satellite radar is more affected by the high clouds, which
482 corresponds to the large LWC at ~200 to 300 hPa. The CAM5 GCM is closer to the
483 C3M profile than to the MICROBASE data below 400 hPa. For IWC, the differences
484 among the two observations and model are relatively small.

485

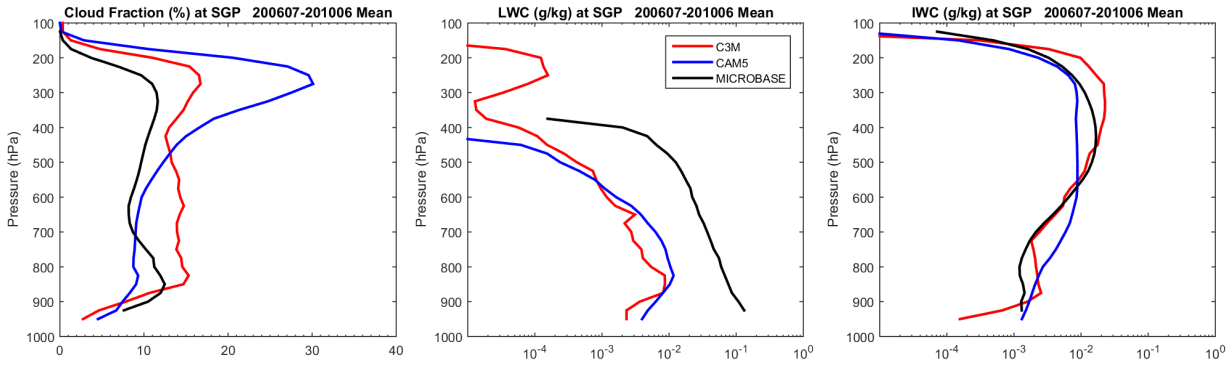

486

487 Figure 10: 4-year (July 2006 to June 2010) mean profiles of cloud fraction (left), LWC (middle)
488 and IWC (right) at SGP site or the closest grid. Blue line is from CAM5 GCM, red line is from
489 C3M merged satellite retrieval, black line is from MICROBASE ground retrieval.

490

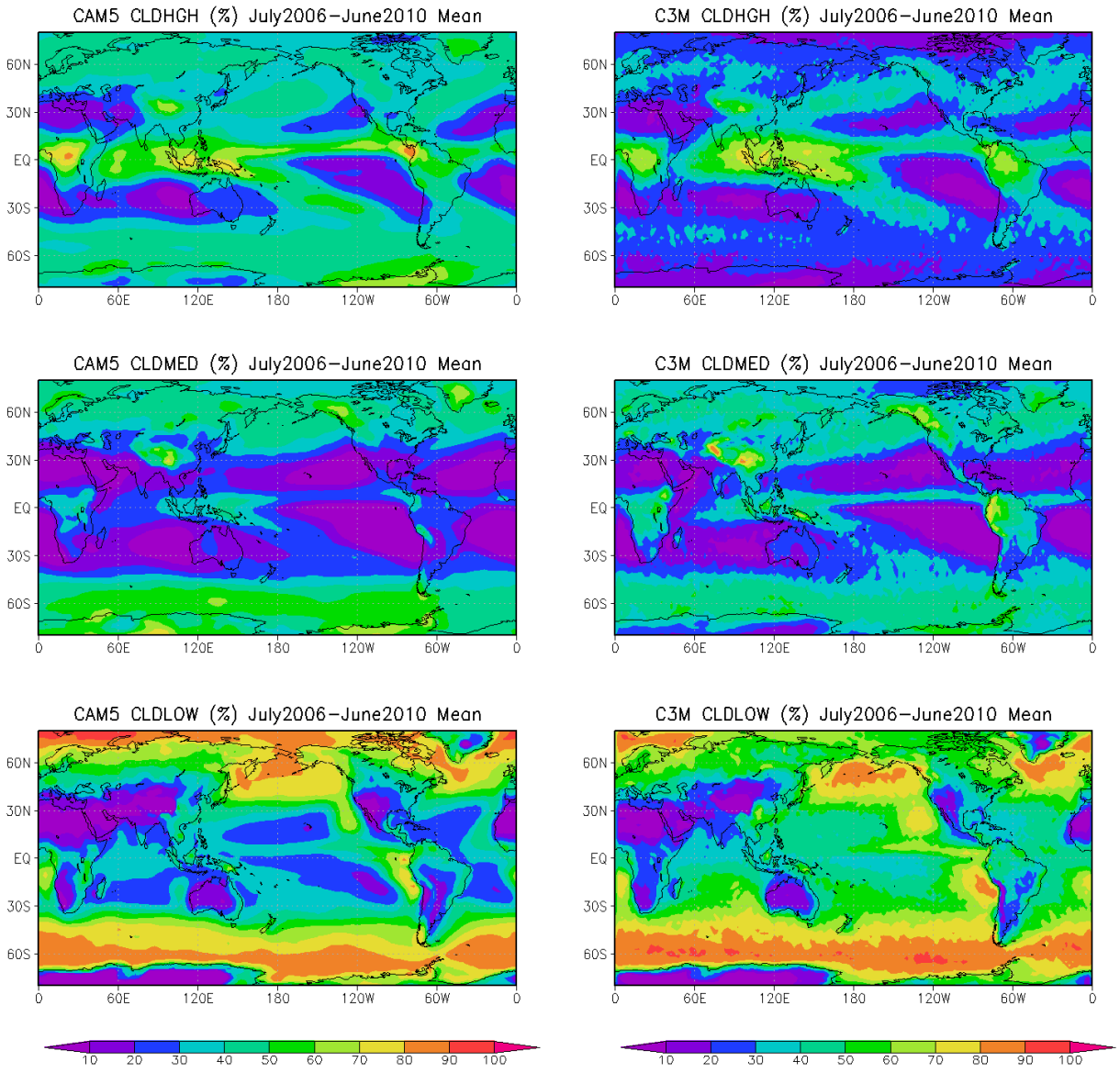

491

492 Figure 11: 4-year (July 2006 to June 2010) mean total high- (top), middle- (middle) and low-
493 (bottom) cloud fraction in CAM5 GCM (left) and C3M merged satellite retrieval (right).

494

495 Despite the large uncertainties in cloud retrievals of LWC and IWC, the model
496 biases of the underestimation of low cloud fraction and overestimation of high cloud
497 fraction in SCAM5 are valid in the CAM5 GCM at SGP from using both satellite-based

498 and ground-based datasets. Therefore, we only compare cloud fractions in CAM5 and
499 C3M for the global distribution of clouds. The high-, mid- and low-cloud fractions from
500 CAM5 and C3M are shown in Figure 11. CAM5 overestimates high-cloud especially in
501 mid- to high-latitude. For mid-cloud, it simulates more clouds in high-latitude but less in
502 the tropics. For low-cloud, CAM5 significantly underestimates cloud fraction over
503 tropical oceans. The global mean fraction of high-, mid- and low-clouds in CAM5 is
504 38.0%, 26.8% and 43.8%, respectively, comparing to 30.2%, 28.4% and 50.3% in C3M.
505 These model biases are overall consistent with SCM and GCM biases at SGP that were
506 described before.

507

508 **5. Summary and Discussion**

509 Background data, error covariance matrix and constraint variables are three
510 important sources of uncertainties (elements) in 3DCVA to derive the large-scale forcing
511 data required by LES/CRM/SCM. We described an ensemble approach of 3DCVA using
512 six background data, five error covariance matrices and three constraint variables
513 (precipitation), in total 90 members. The ensemble approach quantifies the uncertainties
514 of the large-scale forcing data. The results show that all the three elements of the
515 ensemble 3DCVA have considerable impact to the analyzed large-scale forcing data,
516 especially to the vertical velocity and advective tendencies. Among the three elements,
517 background data have the largest impact on the forcing data, while precipitation has
518 relatively larger impact to the horizontal moisture advection.

519 With the uncertainty from the large-scale forcing data calculated and the
520 uncertainty of observed clouds estimated, this study compared the simulated clouds in the
521 SCAM5 with MICROBASE cloud retrievals. We found that SCAM5 overestimates high-
522 clouds while underestimates low-clouds, and it underestimates LWC but overestimates
523 IWC slightly. It also misses some cloud events. Most of these model biases are larger
524 than the uncertainty from large-scale forcing data plus uncertainty from observations,
525 indicating that these biases are "true" model errors. These cloud biases are shown to be
526 consistent with the model biases of surface and TOA radiative fluxes.

527 The applicability of the SCM results at the SGP in the March 2000 IOP to the
528 global model is examined by comparing CAM5 GCM results with the C3M satellite
529 retrievals. We show consistent model biases in cloud fraction: CAM5 overestimates high
530 clouds and underestimates low clouds. These results indicate that most of the GCM
531 biases are caused by physical parameterizations rather than large-scale dynamics, and that
532 the SCM simulations forced by the ensemble large-scale forcing data can be used to
533 further diagnose the cause of model errors in its physical parameterizations.

534 While the ensemble forcing provides a way to estimate the uncertainties in the
535 large-scale forcing data, we point out that the specified uncertainties in the 3DCVA can
536 be improved. This is especially true for the uncertainties in the input data of the
537 constraint variables. The current method only uses uncertainties in the precipitation
538 constraint that is scaled against the best estimate precipitation. More sophisticated
539 specification requires knowledge of the spatial structure of the precipitation uncertainties
540 as well as uncertainties in other constraint variables. With this caveat in mind, we
541 believe the variationally constrained ensemble of large-scale forcing data described in

this paper can be used to more confidently identify and quantify model errors from LES/CRM/SCM.

Acknowledgement: This research is supported by the Biological and Environmental Research Division in the Office of Sciences of the US Department of Energy (DOE), and by the National Science Foundation, to the Stony Brook University. Work at LLNL was supported by the DOE Atmospheric Radiation Measurement (ARM) program and performed under the auspices of the U. S. Department of Energy by Lawrence Livermore National Laboratory under contract No. DE-AC52-07NA27344. The 3DCVA source code and the data are available from the authors upon request (tang32@llnl.gov).

References

Barnes, S. L. (1964), A Technique for Maximizing Details in Numerical Weather Map Analysis, *Journal of Applied Meteorology*, *3*(4), 396-409.

Benjamin, S. G., et al. (2004), An Hourly Assimilation–Forecast Cycle: The RUC, *Monthly Weather Review*, *132*(2), 495-518.

Bretherton, C. S., and S. Park (2009), A New Moist Turbulence Parameterization in the Community Atmosphere Model, *Journal of Climate*, *22*(12), 3422-3448.

Dee, D. P., et al. (2011), The ERA-Interim reanalysis: configuration and performance of the data assimilation system, *Quarterly Journal of the Royal Meteorological Society*, *137*(656), 553-597.

563 Del Genio, A. D., A. B. Wolf, and M.-S. Yao (2005), Evaluation of regional cloud
564 feedbacks using single-column models, *Journal of Geophysical Research: Atmospheres*,
565 *110*(D15), D15S13.

566 Hack, J. J., and J. A. Pedretti (2000), Assessment of Solution Uncertainties in Single-
567 Column Modeling Frameworks, *Journal of Climate*, *13*(2), 352-365.

568 Huang, D., C. Zhao, M. Dunn, X. Dong, G. G. Mace, M. P. Jensen, S. Xie, and Y. Liu
569 (2012), An intercomparison of radar-based liquid cloud microphysics retrievals and
570 implications for model evaluation studies, *Atmos. Meas. Tech.*, *5*(6), 1409-1424.

571 Hume, T., and C. Jakob (2005), Ensemble single column modeling (ESCM) in the
572 tropical western Pacific: Forcing data sets and uncertainty analysis, *Journal of*
573 *Geophysical Research: Atmospheres*, *110*(D13).

574 Jiang, J. H., et al. (2012), Evaluation of cloud and water vapor simulations in CMIP5
575 climate models using NASA "A-Train" satellite observations, *Journal of Geophysical*
576 *Research: Atmospheres*, *117*(D14), D14105.

577 Kato, S., et al. (2011), Improvements of top-of-atmosphere and surface irradiance
578 computations with CALIPSO-, CloudSat-, and MODIS-derived cloud and aerosol
579 properties, *Journal of Geophysical Research: Atmospheres*, *116*(D19), D19209.

580 Khairoutdinov, M., and Y. Kogan (2000), A New Cloud Physics Parameterization in a
581 Large-Eddy Simulation Model of Marine Stratocumulus, *Monthly Weather Review*,
582 *128*(1), 229-243.

583 Khairoutdinov, M., and D. A. Randall (2003), Cloud Resolving Modeling of the ARM
584 Summer 1997 IOP: Model Formulation, Results, Uncertainties, and Sensitivities, *Journal*
585 *of the Atmospheric Sciences*, *60*(4), 607-625.

586 Klein, S. A., et al. (2009), Intercomparison of model simulations of mixed-phase clouds
587 observed during the ARM Mixed-Phase Arctic Cloud Experiment. I: single-layer cloud,
588 *Quarterly Journal of the Royal Meteorological Society*, *135*(641), 979-1002.

589 Kobayashi, S., et al. (2015), The JRA-55 Reanalysis: General Specifications and Basic
590 Characteristics, *Journal of the Meteorological Society of Japan. Ser. II*, *93*(1), 5-48.

591 Lin, X., and R. H. Johnson (1996), Kinematic and Thermodynamic Characteristics of the
592 Flow over the Western Pacific Warm Pool during TOGA COARE, *Journal of the*
593 *Atmospheric Sciences*, *53*(5), 695-715.

594 Mesinger, F., et al. (2006), North American Regional Reanalysis, *Bulletin of the*
595 *American Meteorological Society*, *87*(3), 343-360.

596 Minnis, P., et al. (2008), Near-real time cloud retrievals from operational and research
597 meteorological satellites, paper presented at Proc. SPIE Europe Remote Sens, Cardiff,
598 Wales, UK, , 15-18 September.

599 Morrison, H., and A. Gettelman (2008), A New Two-Moment Bulk Stratiform Cloud
600 Microphysics Scheme in the Community Atmosphere Model, Version 3 (CAM3). Part I:
601 Description and Numerical Tests, *Journal of Climate*, *21*(15), 3642-3659.

602 Neale, R. B., et al. (2012), Description of the NCAR Community Atmosphere Model
603 (CAM 5.0), *NCAR Technical Note Rep. NCARTN-4861STR*, 274 pp.

604 Ooyama, K. V. (1987), Scale-Controlled Objective Analysis, *Monthly Weather Review*,
605 *115*(10), 2479-2506.

606 Park, S., and C. S. Bretherton (2009), The University of Washington Shallow Convection
607 and Moist Turbulence Schemes and Their Impact on Climate Simulations with the
608 Community Atmosphere Model, *Journal of Climate*, *22*(12), 3449-3469.

609 Rienecker, M. M., et al. (2011), MERRA: NASA's Modern-Era Retrospective Analysis
610 for Research and Applications, *Journal of Climate*, *24*(14), 3624-3648.

611 Saha, S., et al. (2010), The NCEP Climate Forecast System Reanalysis, *Bulletin of the*
612 *American Meteorological Society*, *91*(8), 1015-1057.

613 Schumacher, C., M. H. Zhang, and P. E. Ciesielski (2007), Heating Structures of the
614 TRMM Field Campaigns, *Journal of the Atmospheric Sciences*, *64*(7), 2593-2610.

615 Schumacher, C., P. E. Ciesielski, and M. H. Zhang (2008), Tropical Cloud Heating
616 Profiles: Analysis from KWAJEX, *Monthly Weather Review*, *136*(11), 4289-4300.

617 Su, H., et al. (2013), Diagnosis of regime-dependent cloud simulation errors in CMIP5
618 models using "A-Train" satellite observations and reanalysis data, *Journal of*
619 *Geophysical Research: Atmospheres*, *118*(7), 2762-2780.

620 Tang, S., and M. Zhang (2015), Three-dimensional constrained variational analysis:
621 Approach and application to analysis of atmospheric diabatic heating and derivative
622 fields during an ARM SGP intensive observational period, *Journal of Geophysical*
623 *Research: Atmospheres*, *120*(15), 7283-7299.

624 Xie, S., et al. (2002), Intercomparison and evaluation of cumulus parametrizations under
625 summertime midlatitude continental conditions, *Quarterly Journal of the Royal*
626 *Meteorological Society*, *128*(582), 1095-1135.

627 Xie, S., R. T. Cederwall, and M. Zhang (2004), Developing long-term single-column
628 model/cloud system–resolving model forcing data using numerical weather prediction
629 products constrained by surface and top of the atmosphere observations, *Journal of*
630 *Geophysical Research*, *109*(D1).

631 Xie, S., et al. (2005), Simulations of midlatitude frontal clouds by single-column and
632 cloud-resolving models during the Atmospheric Radiation Measurement March 2000

633 cloud intensive operational period, *Journal of Geophysical Research: Atmospheres*,
634 *110*(D15), D15S03.

635 Xie, S., S. A. Klein, M. Zhang, J. J. Yio, R. T. Cederwall, and R. McCoy (2006),
636 Developing large-scale forcing data for single-column and cloud-resolving models from
637 the Mixed-Phase Arctic Cloud Experiment, *Journal of Geophysical Research*, *111*(D19).

638 Xie, S., T. Hume, C. Jakob, S. A. Klein, R. B. McCoy, and M. Zhang (2010a), Observed
639 Large-Scale Structures and Diabatic Heating and Drying Profiles during TWP-ICE,
640 *Journal of Climate*, *23*(1), 57-79.

641 Xie, S., et al. (2010b), CLOUDS AND MORE: ARM Climate Modeling Best Estimate
642 Data, *Bulletin of the American Meteorological Society*, *91*(1), 13-20.

643 Xie, S., Y. Zhang, S. E. Giangrande, M. P. Jensen, R. McCoy, and M. Zhang (2014),
644 Interactions between Cumulus Convection and Its Environment as Revealed by the
645 MC3E Sounding Array, *Journal of Geophysical Research: Atmospheres*, 2014JD022011.

646 Xu, K.-M., et al. (2002), An intercomparison of cloud-resolving models with the
647 atmospheric radiation measurement summer 1997 intensive observation period data,
648 *Quarterly Journal of the Royal Meteorological Society*, *128*(580), 593-624.

649 Xu, K.-M., et al. (2005), Modeling springtime shallow frontal clouds with cloud-
650 resolving and single-column models, *Journal of Geophysical Research: Atmospheres*,
651 *110*(D15).

652 Zhang, M., and J. Lin (1997), Constrained Variational Analysis of Sounding Data Based
653 on Column-Integrated Budgets of Mass, Heat, Moisture, and Momentum: Approach and
654 Application to ARM Measurements, *Journal of the Atmospheric Sciences*, *54*(11), 1503-
655 1524.

656 Zhang, M., J. Lin, R. T. Cederwall, J. J. Yio, and S. C. Xie (2001), Objective Analysis of
657 ARM IOP Data: Method and Sensitivity, *Monthly Weather Review*, *129*(2), 295-311.

658 Zhang, M., et al. (2005), Comparing clouds and their seasonal variations in 10
659 atmospheric general circulation models with satellite measurements, *Journal of*
660 *Geophysical Research: Atmospheres*, *110*(D15), D15S02.

661 Zhang, M., C. S. Bretherton, P. N. Blossey, S. Bony, F. Brient, and J.-C. Golaz (2012),
662 The CGILS experimental design to investigate low cloud feedbacks in general circulation
663 models by using single-column and large-eddy simulation models, *Journal of Advances*
664 *in Modeling Earth Systems*, *4*(4), M12001.

665 Zhao, C., et al. (2012), Toward understanding of differences in current cloud retrievals of
666 ARM ground-based measurements, *Journal of Geophysical Research: Atmospheres*,
667 *117*(D10), D10206.

668 Zhao, C., S. Xie, X. Chen, M. P. Jensen, and M. Dunn (2014), Quantifying uncertainties
669 of cloud microphysical property retrievals with a perturbation method, *Journal of*
670 *Geophysical Research: Atmospheres*, *119*(9), 2013JD021112.

671

672